



**FACULTY
OF MATHEMATICS
AND PHYSICS**
Charles University

MASTER THESIS

Marek Bíroš

Study of the rare B -meson decays with the ATLAS experiment

Institute of Particle and Nuclear Physics

Supervisor of the master thesis: RNDr. Pavel Řezníček, Ph.D.

Study programme: Physics

Study branch: Nuclear and Subnuclear Physics

Prague 2020

Title: Study of the rare B -meson decays with the ATLAS experiment

Author: Marek Bíroš

Institute: Institute of Particle and Nuclear Physics

Supervisor: RNDr. Pavel Řezníček, Ph.D., Institute of Particle and Nuclear Physics

Abstract:

The rare $B_d^0 \rightarrow K^{*0}(892)\mu\mu$ decay is one of the B-physics channels sensitive to Beyond Standard Model effects. The potential deviation from Standard Model predictions could be observed in the angular distribution of this decay. The work compiles several sub-tasks at the initial stage of this complex analysis: decay angles fit validation and signal event preselection. The fit functions used in the analysis are verified on generated toy Monte Carlo data. Ranges of parameters, for which are these functions positive, are established and within this parametric space, the testing of possible intrinsic fit biases is evaluated. A dependence of the fit bias with respect to the collected number of events (expected in Run 2 as well as at HL-LHC) and to the different signal-to-background ratio is studied. The second part of the thesis deals with processing of raw reconstructed data from the detector into n-tuples resulting in a more compact dataset that would be used in the final analysis. Within the process, baseline cuts are applied in order to minimize size of final datasets by reducing majority of background events. The procedure is validated on full Monte Carlo simulated data, applying final event selection taken from the Run-1 analysis.

Keywords: ATLAS, LHC, rare B -meson decays, angular analysis, maximum likelihood fit validation, event selection

Contents

Introduction	1
1 The ATLAS Experiment	2
1.1 Large Hadron Collider	2
1.2 The ATLAS Detector	3
1.3 The ATLAS Upgrades Summary	3
1.4 Particle Detection with ATLAS	4
1.4.1 The Decay Reconstruction	5
2 The Decay $B_d^0 \rightarrow K^* \mu^+ \mu^-$ in the ATLAS	7
2.1 Flavour Changing Neutral Currents	8
2.2 Angular Analysis of $B_d^0 \rightarrow K^* \mu^+ \mu^-$	8
2.2.1 Decay Parametrization	8
2.2.2 Background Processes	8
2.2.3 Angular observables	9
2.3 Latest Overview of Measurements	10
3 Toy Monte Carlo Studies of the Angular Fit	12
3.1 Expected SM Values	12
3.2 Positive Range of Fitted Functions	12
3.3 Used Methodology	13
3.4 Results	15
3.4.1 Summary of the Toy-MC Studies	15
3.4.2 Plots of Number of Successfully Passed Fits and the Fit Error for F_L with $r=1$ and the Run 1 acceptance	17
3.4.3 Plots of Number of Successfully Passed Fits and the Fit Error for S_5 with $r=1$ and the Run 1 acceptance	18
3.4.4 Pull Plots for F_L with $r=1$ and the Run 1 acceptance	19
3.4.5 Pull Plots for S_5 with $r=1$ and the Run 1 acceptance	20
4 Events Preselection	21
4.1 Used Software	21
4.2 Selection Criteria	23
4.2.1 Baseline Cuts	23
4.2.2 Run 1 Cuts	23
4.3 Results	24
4.3.1 Application of Selection Criteria	24
4.3.2 Background Yield Estimation	25
Conclusion	28
A Appendices	29
A.1 CERN Linux and Batch Service	29
A.1.1 Technical Manual	30
Bibliography	32

Introduction

This thesis presents initial stages of the Run 2 (data collected in years 2015–2018) analysis of the decay $B_d^0 \rightarrow K^{*0}(892) \mu^+ \mu^-$ ($B_d^0 \rightarrow K^* \mu \mu$ from now on) with the ATLAS experiment. Decays including FCNC transition of b quark into s quark (as $B_d^0 \rightarrow K^* \mu \mu$) are forbidden at the tree level in the Standard Model (SM) and undergo through loops only. In extensions of the SM, new particles may occur inside the loops and manifest themselves in the matrix element that could be measured in the branching fraction of the decay or in the distribution of decay angles between momenta of the final-state particles. The most recent results of the angular distribution measurement was provided by the LHCb collaboration. Results from their analysis of Run 1 (2011–2012) are in a good agreement with SM predictions except of the local deviation in one of the observables (P'_5 , see definition later) with a significance at the level of 3 standard deviations. Recent update of the analysis with data collected in 2016 specifies the deviation at the similar level and therefore more data are needed in order to confirm or disprove the discrepancy between the measurements and the theoretical predictions.

The thesis is organized as follows. The first chapter briefly introduces the ATLAS detector, realized and planned upgrades and principles of particle detection. A necessary theoretical background for the $B_d^0 \rightarrow K^* \mu \mu$ decay is introduced in the second chapter. The rest of the thesis is devoted to author's original results: the validation of the fit of the decay angles distribution using toy Monte Carlo (MC) simulations (the third chapter) and processing of raw reconstructed data from the detector into n-tuples used in the final analysis (the fourth chapter).

The third chapter starts with determination of valid fit-parameters range. Due to the complexity of the fit and relatively low number of expected signal events in real data, the fit suffers from intrinsic biases. A dependence of the fit bias with respect to the collected number of events measured in Run 1, expected in Run 2 and at HL-LHC, and to the different signal-to-background ratio is studied with and without effects of the detector. This text presents results only for the fit involving parameter P'_5 (where LHCb observed the deviation from SM prediction), however, all combinations of the fit-parameters were tested.

The functionality of the n-tuple maker is demonstrated in the last chapter on processing of limited-size of fully simulated Monte Carlo samples (including full simulation and reconstruction chain of the ATLAS experiment). The tests are based on application of set of cuts from the analysis of the ATLAS Run-1 data.

Useful technical details and a short manual of CERN linux and batch service are summarized in the appendix.

1. The ATLAS Experiment

The ATLAS experiment [1] is one of major particle experiments in CERN. To be more specific, ATLAS is the biggest general-purpose particle detector on the world with height of 25 m and length of 44 m. The acronym ATLAS stands for A Toroidal LHC ApparatuS. The ATLAS detector measures mainly proton-proton but also proton-lead and lead-lead collisions in the Large Hadron Collider. The main aims of the experiment were established to find Higgs boson, search for decays of supersymmetric particles, gravitons and the minimal supersymmetric extension of the SM Higgs mechanism. The first one was fulfilled in 2012, however measurements of the Higgs boson's properties still continue.

1.1 Large Hadron Collider

The Large Hadron Collider (LHC) is the world's largest and most powerful particle accelerator. It is a 27-kilometre long synchrotron devoted to acceleration of protons and lead nuclei. Two beams travel in opposite directions in separate beam pipes with ultrahigh vacuum and are made to collide at four locations around the accelerator ring. Each interaction point is enveloped by one of four great particle detectors – ATLAS, CMS, ALICE and LHCb.

Detectors ATLAS, CMS and ALICE are built symmetrically around the interaction point. LHCb is a single arm forward detector. ATLAS and CMS, A Toroidal LHC ApparatuS and the Compact Muon Solenoid, respectively, are general purpose detectors, so called, discovery machines. A Large Ion Collider Experiment (ALICE) is a heavy-ion detector, focusing on lead lead collisions. It is designed to study the physics of quark-gluon plasma, a strongly interacting phase of matter at extreme energy densities. The LHC beauty (LHCb) is specialized in heavy flavour measurements, in particular involving b-hadrons, primarily the measurement of CP violation parameters.

In addition, there are three less known LHC-experiments: TOTEM, LHCf and MoEDAL. TOTAl Elastic and diffractive cross section Measurement is designed to take precise measurements of protons emerging from collisions at small angles. Since TOTEM is placed in the CMS cavern, both collaborations coordinate the usage of their detectors to perform combined measurements. The LHC-forward experiment uses particles thrown forward by collisions in the ATLAS interaction point as a source to simulate cosmic rays in laboratory conditions. The LHCb cavern hosts the Monopole and Exotics Detector that searches directly the magnetic monopole – a hypothetical particle with a magnetic charge. MoEDAL also looks for Beyond Standard Model (BSM) physics, particularly highly ionizing Stable Massive Particles (SMPs).

The accelerator ring consists of superconducting magnets with several accelerating structures to boost the energy of particles along the way. There are two types of magnet systems: dipole magnets which bend the beams, and quadrupole magnets which focus them. Protons are injected into LHC from the pre-acceleration chain: accelerated to energy of 50 MeV in Linac 2, to energy of 1.4 GeV in Booster, to 25 GeV in PS and finally to 450 GeV in SPS. After that, they are injected inside LHC where they reach the maximal energy of 13 TeV.

1.2 The ATLAS Detector

The ATLAS detector consists from four main subsystems: inner detector, calorimetry, muon spectrometer and trigger.

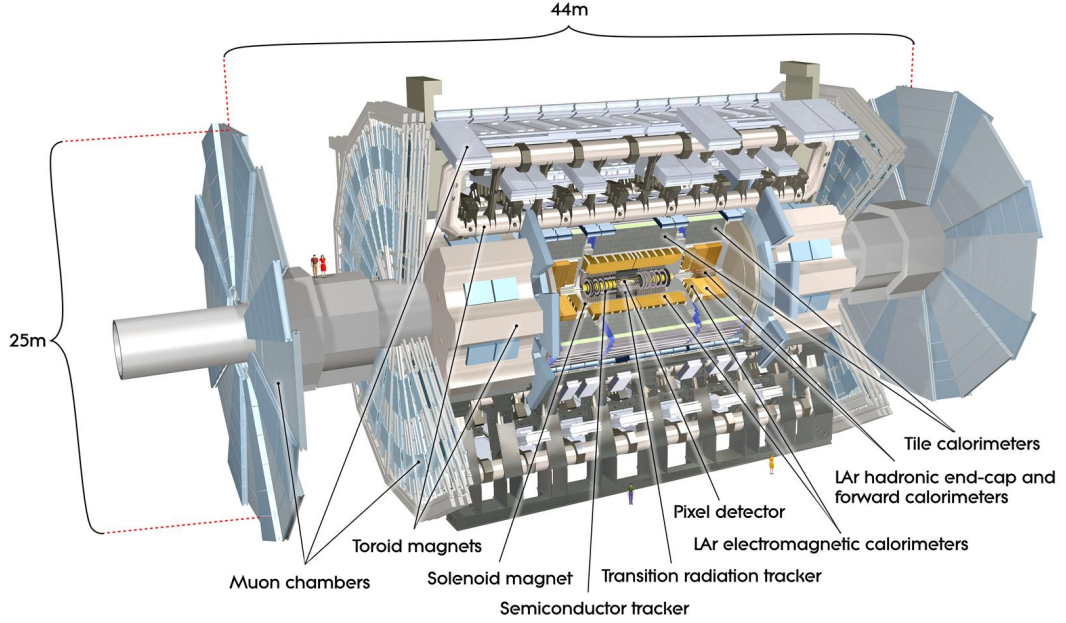


Figure 1.1: Scheme of the ATLAS detector [1].

Inner Detector (ID) measures tracks of charged particles. The system of calorimeters measures deposited energy of particles passing through it. The outermost layer of the detector is devoted for muon detection since most of particles stop in the calorimeters and only muons continue to the muon spectrometer. The number of proton collisions is enormous, however recording possibilities are limited. Thus one has to reduce amount of data which will be saved to later analysis and that is a purpose of the trigger system. Individual parts of detector are described [1] according to their first construction in 2008. Performed updates are discussed in section 1.3. Section 1.4 presents ATLAS mechanism of particle detection and more specific with respect to the $B \rightarrow K^* \mu \mu$ analysis in section 1.4.1.

1.3 The ATLAS Upgrades Summary

In order to achieve the best possible conditions for physics analysis the ATLAS detector is in continual development. Small improvements are performed during long shutdowns of LHC when the data-taking is stopped. The majority of changes are connected to the detector resolution and its radiation resistance. Especially the innermost parts of detector are highly sensitive to the radiation damage that increases with the increment of the LHC luminosity. The innovations are limited by accessible free space in the cavern for installation and by price.

The first considerable upgrade was implemented during first long shutdown (LS 1) in 2013-2014. The IBL (Insertable B-Layer) was installed as a new innermost layer for the pixel detector. It was inserted between the beam pipe and the current pixel B-layer¹, back then the innermost pixel layer, at a radius of 3.2 cm. Thus an installation of a new beam pipe with a radius of 2.35 cm was necessary. The new layer consists of 14 staves [2] which are arranged in a turbine-like fashion. Each stave contains 12 double-chip sensors in planar technology and 8 single-chip sensors in 3D technology. The IBL provides a significant improvement to the vertexing, tracking and also b-tagging of the ATLAS detector.

For Run 2 the Level-2 trigger and the event filter were merged into new High-Level Trigger (HLT) that uses entire detector data but reads only minimal amount to reach decision. [3] The rate of saved events increased from 200 Hz to 1000 Hz.

Currently (LS 2 2018-2021) several accelerator updates are being undertaken in order to achieve higher luminosity. Integration of the Linac4 into the LHC injector complex, increment of the the PS Booster energy, reduction of the beam emittance, and upgrade of the collider collimation system are in progress. Thus the peak luminosity will increase to reach $(2 - 3) \times 10^{34} \text{ cm}^{-2}\text{s}^{-1}$ corresponding to 55 to 80 interactions per pp crossing. [4] The integrated luminosity will be $300 - 400 \text{ fb}^{-1}$. Higher number of events requires improvement of the present L1 trigger. This will be achieved by introducing a new tracking and trigger device in the inner layer of the forward muon spectrometer, and a new trigger read-out boards and higher trigger granularity in the electromagnetic and forward calorimeters. This upgrade will improve among other things, the event selection (τ , b tagging) and enable ATLAS to establish limits on quartic gauge coupling $\gamma\gamma WW$.

Much more significant upgrades are planned during the LS 3 (2024-27) [5], preparing the ATLAS detector's cooperation with the expected conditions at HL-LHC (High Luminosity LHC). The instantaneous luminosity will be in range $(5 - 7) \times 10^{34} \text{ cm}^{-2}\text{s}^{-1}$ which corresponds to 140 – 200 pile-up events. Total integrated luminosity will reach 3,000 fb^{-1} . The HL-upgrade would have the highest effect on the performance of ID (especially, the gas-based TRT) that would suffer from radiation damage and high occupancy. Therefore, the the whole ID will be replaced by a new, all-silicon Inner Tracker (ITk) [5]. Hence aging of the calorimetry system and the muon spectrometer (around 20 years of running), they will require restoration as well. The granularity of Tile Calorimeter will have to be increased. The performance of the existing MDT chambers together with the new small wheels, upgraded in LS 2, appears to be sufficient for operation at the HL-LHC. However, the MDT readout electronics will have to be adapted to the new trigger scheme and to the increased hit rates.

1.4 Particle Detection with ATLAS

General purpose detectors, such as ATLAS, are devoted to the broadest examination of collisions in the interaction point; they should distinguish which

¹Reference of the innermost layer as a B-layer comes from its ability to distinguish if particle came from the primary vertex or from a shifted secondary vertex (e.g. b -hadron decay) more precisely than other ATLAS parts.

particles have interacted and determine their properties (four-momenta, charge, lifetime, ...). That could be achieved by precise cooperation of all ATLAS parts.

Charged particles could interact with the inner detector by EM force and cause ionization or excitation of electrons in its material. This signal can be collected and allows to reconstruct a map of hits in the ID and build the particles tracks. Their momenta are established from measurements of the trajectories bending in the magnetic field. The orientation of the bending provides information about charge of particles. Since neutral particles do not interact electromagnetically, they fly through the ID unseen.

A better particle recognition stands on the way how particles deposit their energy in the calorimeters. Losses caused by bremsstrahlung are inversely proportional to particle mass square. The bremsstrahlung initiates and develops electromagnetic showers and therefore the lightest particles detected in ATLAS, electrons, stop in the calorimeter first. The electromagnetic cascades (showers) are composed from electrons, positrons and photons. The EM shower could be also created by photons, however photons and electrons could be easily distinguished because photons do not interact in the ID. Heavier partners of electrons, muons, have so small energy losses (without bremsstrahlung they do not initiate EM showers) that muons with higher energy (typically more than 2 GeV, but it depends on the muon direction) simply do not stop in the calorimeter volume but continue to the MS and out of the detector. The MS measures their tracks based on similar principle as the measurement in the ID and their momenta are established by combination of their tracks in the ID and in the MS. Hadrons interact with matter except of EM by strong interaction as well. That means that although they have higher masses than muons, so their bremsstrahlung is negligible and ionisation is similar to muons, they can loose energy by interaction with nuclei and create hadronic showers as well. ATLAS can use differences in particles ionisation for identification, however that works on the low energy level, $p_T < 0.5$ GeV and hence it can not be used in our study. This is more discussed in the section 1.4.1. The hadron collisions produce more often jets rather than isolated hadrons. Jets consist of many hadrons flying in the same direction. They are produced when a high-energy quark or gluon births in the primary collision and because partons can not stay alone in a state with non-zero colour, they hadronize and result in jets. Taons decay before they could interact with the detector and produce electrons, muons or jets, together with neutrinos. Neutrinos are undetectable for the ATLAS since they can interact by weak interaction only.

This chapter is summary illustrated in Fig. 1.2.

1.4.1 The Decay Reconstruction

The final state of the studied decay consists from a kaon, a pion and two muons. Muons are measured in the ID and in the MS and hadrons in the ID and in the calorimeters as discussed above. As was suggested, the ATLAS particle identification is rather not very usable for hadrons within the kinematic range of the studied decay, so the output from ATLAS contains momenta of two oppositely charged hadrons without any information if K^* decayed into $K^+\pi^-$ or \bar{K}^* into $K^-\pi^+$ or if it is some background composed of other hadronic tracks. This is solved by application of the mass hypothesis on the reconstructed mass of K^* .

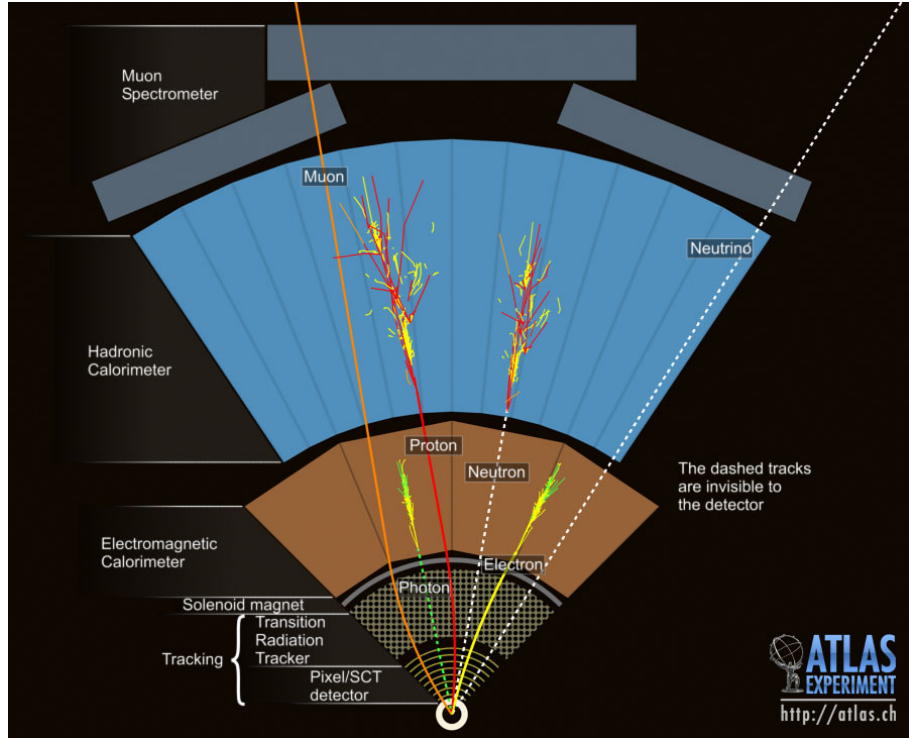


Figure 1.2: Scheme of the particle detection with ATLAS [6].

Firstly the reconstruction of both cases is evaluated; the invariant mass of kaon is assigned to the positive hadron and the pion mass to the negative (resp. vice versa) and the proper four-momenta and the invariant mass of the K^* (resp. \bar{K}^*) is computed. The mass distribution of the K^* is theoretically described by the Breit-Wigner distribution with mean 894 MeV and half-width of 50 MeV [7]. Finally both the reconstructed m_{K^*} and $m_{\bar{K}^*}$ are tested whether they fit in the interval 894 ± 50 MeV. In events with both masses or only one mass laying in the interval we choose the case with mass closer to the mean. If neither one mass fits in the interval, the event is excluded from the analysis.

According to the MC simulations, this approach leads to a 10% error of misidentification of the B_d^0 and \bar{B}_d^0 decays. This effect was in details investigated in Ref. [8].

2. The Decay $B_d^0 \rightarrow K^* \mu^+ \mu^-$ in the ATLAS

One of indirect paths for searching a new physics beyond Standard Model is the precise measurement of higher order processes which is the task for flavour physics. New particles could occur in the loops and manifest themselves in the matrix element. The matrix element of decay can be measured only indirectly, e.g. can be extracted from a cross section or from an angular distribution of its products. The flavour physics mainly focuses on looking for flavour changing neutral currents and lepton flavour violation as they seem as the most promising physical channels that could potentially include a substantial trace to a new BSM physics. A big part of flavour physics, the B -physics, is observation of hadrons containing the bottom quark. Hadrons containing the b -quark are the most massive since the top quark decays before it could form a hadron. The large mass of b -quark might increase the coupling to new particles predicted by the BSM theories. B -hadrons are relatively stable so they could fly up to several millimeters in ATLAS before they decay. This distance is enough to distinguish their decay from the primary pp collisions.

This thesis is connected with one of the ATLAS B -physics analysis groups that is specialized in semileptonic rare decays. Our subgroup is focused on the angular distribution of $B_d^0 \rightarrow K^* \mu^+ \mu^-$. We also cooperate with an another subgroup trying to reveal a discrepancy of $K^* \mu \mu$ and $K^* e e$ branching ratios. Direct decays of B -meson into K^* and a pair of leptons are prohibited at the tree level therefore they are appropriate to a precise measurement of loop decays. The decays can be described by two types of loop diagrams – the penguin and the box one (shown in Fig. 2.1). The $B \rightarrow K^* \mu \mu$ decay rate is thus very low; the branching ratio is only $(9.4 \pm 0.5) \times 10^{-7}$ [7]. Although the $K^* \mu \mu$ decay is very rare, it is nowadays measurable thanks to the enormous LHC luminosity. The first ATLAS analysis of the decay in Run 1 found only slightly above 300 signal events [9].

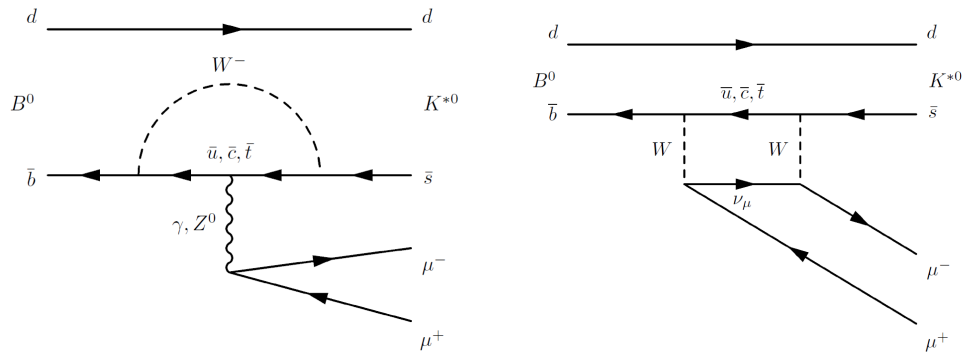


Figure 2.1: Loop Feynman diagrams of the $B_d^0 \rightarrow K^* \mu^+ \mu^-$ decay. The left one is usually referred as a penguin diagram, the right one as a box diagram.

2.1 Flavour Changing Neutral Currents

Flavour changing neutral currents (FCNCs) denote processes changing the flavour of a fermion current without altering its electric charge. In the Standard Model they can occur only on loop level so they are much more suppressed with compare to flavour changing charged current (FCCC) which can occur at tree level as well. The rarity of FCNCs is essential to their sensitivity to new physics. Suppression of the SM contributions let us measure even very small BSM contributions that would be undetectable in the higher rate of FCCC processes. New particles may occur in the loops or can mediate FCNC at tree level with small couplings (their suppression is necessary for an agreement with observations).

A typical example for FCNC decay is the b to s transition included in the studied decay.

2.2 Angular Analysis of $B_d^0 \rightarrow K^* \mu^+ \mu^-$

2.2.1 Decay Parametrization

The four kinematic variables are used for parametrization of the angular distribution: q^2 (squared invariant mass of the dimuon pair), $\cos \theta_K$, $\cos \theta_L$ and ϕ as is shown in Fig. 2.2.

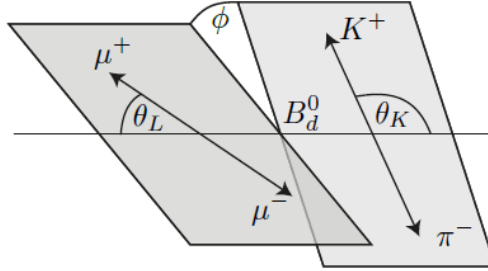


Figure 2.2: Scheme of the ATLAS angular parametrization of the decay [9]. θ_L is defined as the angle between the direction of the μ^+ (μ^-) and the direction opposite to that of the B_d^0 (\bar{B}_d^0) in the dimuon rest frame, θ_K is defined in the K^* (\bar{K}^*) rest frame between the direction of the K^+ (K^-) and the direction opposite to that of the B_d^0 (\bar{B}_d^0) and ϕ is the angle between the planes.

2.2.2 Background Processes

In this section, the known background processes that needs to be considered in the analysis are introduced. There are three types of background events: 1) other decay channels of B_d^0 with the same final state, 2) similar decays that seem like signal for the detector and 3) combinatorial background. The combinatorial background events are created when the detector reconstructed two muons and two hadrons into the a common vertex, however they originated from different decay vertices (a hadron and muon vertex or a partially reconstructed B -decay with an accidental hadron or muon track). This type of background would mostly

vanish for the detector with the ideal spacial resolution. The second type of background would be suppressed with a good particle identification system.

The background studies in general are needed for the event selection and for the investigation of possible contributions of backgrounds decays to the measured angular distribution. Studies of 1) and 2) are typically accomplished using fully simulated MC data while 3) is naturally examined on the real data, out of the signal region, for the final event selection.

Decay channels of B_d^0 with the same final state particles (and reconstructed tracks) as the signal decay :

$$B_d^0 \rightarrow K^*(K\pi)(\overline{\mu\mu}), B_d^0 \rightarrow K\pi(\overline{\mu\mu})$$

Decays with similar final state particles, not distinguishable from signal due to missing hadron identification:

$$B_s^0 \rightarrow \phi(K^+K^-)(\overline{\mu\mu}), \Lambda_b \rightarrow \Lambda(1520)(p\pi^-)\mu^+\mu^-, \Lambda_b \rightarrow p\pi^-\mu^+\mu^-$$

Remarkable components of combinatorial background that could have non-trivial contribution to the angular analysis:

$$B^+ \rightarrow K^+(\overline{\mu\mu}), B^+ \rightarrow \pi^+(\overline{\mu\mu})$$

where $(\overline{\mu\mu})$ stands for possible direct semileptonic decay $(\mu^+\mu^-)$ or the hadronic decay of J/ψ , $\psi(2S)$ or η . Naturally, the CP-conjugated decays are considered as well.

Data are processed in three separate bins according to q^2 : $[0.04 - 2]$ GeV², $[2 - 4]$ GeV², $[4 - 6]$ GeV². The lower edge is limited by muons mass while the upper is limited by a radiative tail from the $B_d^0 \rightarrow K^*J/\psi$ events, significantly contributing for q^2 above 6.0 GeV². A veto of the range $[0.98 - 1.10]$ GeV² is applied, removing contribution from $\phi \rightarrow \mu\mu$ decays.

2.2.3 Angular observables

The angular differential decay rate as a function of q^2 and $\vec{\Omega} \equiv (\cos\theta_K, \cos\theta_L, \phi)$ can be written in many ways. In our analysis we used a form with coefficients representing the helicity or transversity amplitudes (F_L is the fraction of longitudinally polarised K^* mesons and the S_i are angular coefficients which are functions of the real and imaginary parts of the transversity amplitudes of the decay. The forward-backward asymmetry is given by $A_{FB} = 3S_6/4$ [9]. Since these parameters vary with q^2 and the analysis is processed in bins, an average values in bins are calculated):

$$\begin{aligned}
\frac{1}{d\Gamma dq^2} \frac{d^4\Gamma}{d\cos\theta_L d\cos\theta_K d\phi dq^2} = & \frac{9}{32\pi} \left[\frac{3(1-F_L)}{4} \sin^2\theta_K + F_L \cos^2\theta_K \right. \\
& + \frac{1-F_L}{4} \sin^2\theta_K \cos 2\theta_L - F_L \cos^2\theta_K \cos 2\theta_L \\
& + S_3 \sin^2\theta_K \sin^2\theta_L \cos 2\phi + S_4 \sin 2\theta_K \sin 2\theta_L \cos \phi \\
& + S_5 \sin 2\theta_K \sin \theta_L \cos \phi + S_6 \sin^2\theta_K \cos \theta_L \\
& + S_7 \sin 2\theta_K \sin \theta_L \sin \phi + S_8 \sin 2\theta_K \sin 2\theta_L \sin \phi \\
& \left. + S_9 \sin^2\theta_K \sin^2\theta_L \sin 2\phi \right]. \tag{2.1}
\end{aligned}$$

High number of free parameters of the full angular distribution (8) leads to a fit instability, especially in a case with small number of events. Therefore our analysis restricts itself to folded distributions with only 3 free parameters that could be obtained from 2.1 after an application of the symmetries, as a following transformation 2.2. Implementing it in Eq. (2.1) yields the distribution in terms of S_5 (other folded forms can be found in the original paper [9]):

$$f_{S_5}(\vec{\Omega}; F_L, S_3, S_5) : \begin{cases} \phi \rightarrow -\phi & \text{for } \phi < 0 \\ \theta_L \rightarrow \pi - \theta_L & \text{for } \theta_L > \frac{\pi}{2} \end{cases} \tag{2.2}$$

$$\begin{aligned}
f_{S_5}(\vec{\Omega}; F_L, S_3, S_4) = & \frac{9}{8\pi} \left[\frac{3(1-F_L)}{4} \sin^2\theta_K + F_L \cos^2\theta_K + \frac{1-F_L}{4} \sin^2\theta_K \cos 2\theta_\ell \right. \\
& - F_L \cos^2\theta_K \cos 2\theta_\ell + S_3 \sin^2\theta_K \sin^2\theta_L \cos 2\phi \\
& \left. + S_5 \sin 2\theta_K \sin \theta_L \cos \phi \right] \tag{2.3}
\end{aligned}$$

Although the S_i parameters are used in the analysis, their fractions referred as P_i parameters are more useful for comparison with theoretical predictions because of the elimination a strong dependence on hadronic form factors (the greatest source of theoretical uncertainties):

$$P_1 = \frac{2S_3}{1-F_L} \tag{2.4}$$

$$P_2 = \frac{1}{2} \frac{S_6}{1-F_L} \tag{2.5}$$

$$P_3 = -\frac{S_9}{1-F_L} \tag{2.6}$$

$$P'_{j=4,5,6,8} = \frac{S_{i=4,5,7,8}}{\sqrt{F_L(1-F_L)}}. \tag{2.7}$$

2.3 Latest Overview of Measurements

The same angular analysis has been performed except of ATLAS by the BaBar, CMS, LHCb and Belle collaborations. All measurements agreed with

the SM within uncertainties, except the P'_5 parameter which shows a local discrepancy with predictions in some of the q^2 bins. The latest and most relevant results come from LHCb upgrade of Run 1 analysis with data from 2016. The measured deviations of 2.8 and 3.0 of the standard deviation in Run 1 for the q^2 bins $[4,6]$ GeV^2 and $[6,8]$ GeV^2 , respectively, reduces a little to 2.5 and 2.9 σ after the addition of new data which could have two antipodal interpretations. The first approach is that with a higher statistics there is still a remarkable deviation from predictions and therefore some BSM physics can be revealed here. However a more conservative reader would interpret it rather contrariwise that the measurement rejoins the theory (the absolute difference between theory and experiment went down with the new 2016 data). Because of these ambiguous interpretations there is still a huge space for studying this decay in order to confirm one of these hypotheses.

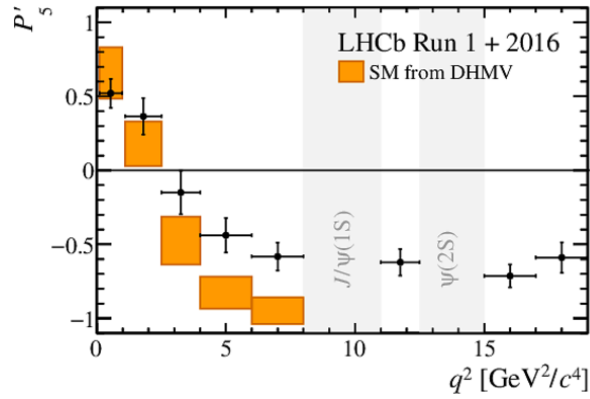


Figure 2.3: Results for the measurement of the P'_5 parameter compared to SM predictions [10].

3. Toy Monte Carlo Studies of the Angular Fit

A very important, however sometimes overlooked part of data analysis is a validation of functions used in the fit. It is a process of generating and fitting MC data in order to establish the stability of the fit and to study possible intrinsic biases of fitted functions. Instead of a full generation of decays coming from the pp collisions and their propagation through the detector, only toy MC samples of angular (and mass) distribution according to the fitted functions are generated for each studied combination of the initial parameters. These samples are fitted and results of the fit are compared with the initial parameters and are averaged for N_{MC} samples. The number of generated signal and background events was based on results of Run 1 for each bin, and the impact of changing number of events (predictions for Run 2 and HL-LHC) and signal-to-background ratio was studied. The validation was processed twice: ignoring effects of the detector and taking into account the acceptance (affecting the angular shapes) from Run 1.

Before the validation it is necessary to introduce values of theoretical predictions for the SM (sec. 3.1) and to establish parameters' space where the functions are positive ($p.d.f. > 0$, see sec. 3.2). The validation strategy and studied variables are presented in sec. 3.3. Results of the validation are presented only for the parameters F_L and S_5 (needed for computation of P'_5 , the parameter where LHCb observed deviation from SM prediction), for the same signal-to-background ratio as was measured in Run 1 ($r = 1$) and the Run 1 acceptance.

3.1 Expected SM Values

In order to test the feasibility of measurement of deviation from the SM, it is necessary to well know the SM prediction. Therefore many theoretical publications analyze properties of $B_d^0 \rightarrow K^* \ell \ell$ decays. The predicted values of tested parameters are also needed for the fit validation since every test (generating and fitting) varies with only one variable while the rest is fixed for the SM values. This approach is based on the expectation that deviations from the SM should be small and simplifies studying of the evolution of multiparametric functions.

The predicted values from the paper [11](Tab. IV) are listed in Tab. 3.1 after transformation of theoretical P -parameters into S -parameters used in the analysis, using Eq. 2.4–2.7. The paper works with two times softer binning and therefore the P -values are firstly weighted-averaged according to the branching ratio into corresponding bins and then transformed from P to S .

3.2 Positive Range of Fitted Functions

Ranges of parameters F_L , S_3 and S_i , where the fitted functions f_i are positive, are established for each q^2 bin. A function passes the positivity criterion for a

	q^2 bin		
	[0.04 – 2.0] GeV ²	[2.0 – 4.0] GeV ²	[4.0 – 6.0] GeV ²
F_L	0.380	0.780	0.698
S_3	7.98×10^{-3}	-1.73×10^{-3}	-9.32×10^{-3}
S_4	0.061	-0.119	-0.214
S_5	0.227	-0.125	-0.343
S_6	-0.341	-0.220	0.292
S_7	2.05×10^{-2}	2.27×10^{-2}	6.70×10^{-2}
S_8	1.33×10^{-3}	5.59×10^{-3}	4.79×10^{-3}
S_9	-3.80×10^{-6}	-6.60×10^{-6}	-4.28×10^{-6}

Table 3.1: Predicted values of parameters in the SM [7].

specific parameter when it had positive values for the whole parametric space of $\bar{\Omega} = (\theta_K, \theta_L, \phi)$ while the rest of parameters are kept on SM values.

Taking into account non-zero effects of the detection process, the fitted functions are multiplied by the detector acceptance (product of polynoms for each angle). The acceptance for Run 2 has not been determined yet, thus the acceptance from Run 1 is used.

In order to cross-check the acceptance is not including any negative shapes in the angular space, the positivity tests were processed both with and without the acceptance. Nevertheless, as expected, both have the same results that are presented in the tab. 3.2.

		q^2 bin		
		[0.04 – 2.0] GeV ²	[2.0 – 4.0] GeV ²	[4.0 – 6.0] GeV ²
f_{S_4}	F_L	0.000 – 0.984	0.020 – 0.970	0.088 – 0.904
	S_3	-0.310 – 0.310	-0.110 – 0.110	-0.150 – 0.150
	S_4	-0.348 – 0.348	-0.295 – 0.295	-0.327 – 0.327
f_{S_5}	F_L	0.056 – 0.960	0.018 – 0.979	0.137 – 0.844
	S_3	-0.240 – 0.310	-0.098 – 0.110	-0.067 – 0.150
	S_5	-0.491 – 0.491	-0.411 – 0.411	-0.443 – 0.443
f_{S_7}	F_L	0.000 – 0.983	0.000 – 0.996	0.004 – 0.981
	S_3	-0.310 – 0.309	-0.110 – 0.110	-0.150 – 0.146
	S_7	-0.479 – 0.479	-0.417 – 0.417	-0.472 – 0.472
f_{S_8}	F_L	0.000 – 0.984	0.000 – 0.996	0.000 – 0.981
	S_3	-0.310 – 0.310	-0.110 – 0.110	-0.150 – 0.150
	S_8	-0.348 – 0.348	-0.295 – 0.295	-0.327 – 0.327

Table 3.2: Range of tested parameters, where the fit functions are positive for the whole angular space of $\bar{\Omega}$.

3.3 Used Methodology

As was mentioned before, the fit behaviour with respect to the number of events and different signal to background ratios was studied. In general, the

fit quality should improve for higher number of data, so number of events from Run 1 analysis ($n = 1$) was compared with a rough expectations for Run 2 ($10\times$ more events, $n = 10$) and for High Luminosity LHC update ($n = 100$) [12]. Based on the similiar analysis of $B_s \rightarrow J/\psi\phi$, no significant changes in signal to background ratios are expected (difference of Run 1 and Run 2 is only a few percent). Nevertheless, rather more extrem values were tested: $2\times$ more background than signal and vice versa respectively: $r = 0.5, r = 2$, which would better demonstrate effects of different ratios on the fit. The more extreme values or r can also better represent possible updates in the event selection procedure, which is likely to happen in the Run 2 and beyond analyses: using multivariate techniques as Boosted Decision Trees (BDT) instead of simple cuts.

Number of measured signal and background events in Run 1:

q^2 bin	n_{sig}	n_{bck}
[0.04, 2.0] GeV ²	128^{+22}_{-22}	122^{+22}_{-21}
[2.0, 4.0] GeV ²	106^{+23}_{-22}	113^{+23}_{-22}
[4.0, 6.0] GeV ²	114^{+24}_{-23}	204^{+26}_{-25}

Table 3.3: Signal and background yields from the Run 1 analysis [9].

The tests were performed for all q^2 bins separately; together 3195 combinations were tested for both cases: with and without detector acceptance. The tested range of parameters were chosen based on Tab. 3.2:

- $F_L \in [0.1, 0.9]$, with step 0.09; ([0.2,0.8] for 4-6 GeV² bin of f_{S_5})
- $S_3 \in [-0.1, 0.1]$, with step 0.02; ([-0.06,0.1] for 4-6 GeV² and [-0.08,0.1] for 2-4 GeV² bin of f_{S_5})
- $S_4 \in [-0.272, 0.272]$, with step 0.068
- $S_5 \in [-0.4, 0.4]$, with step 0.08
- $S_7 \in [-0.4, 0.4]$, with step 0.08
- $S_8 \in [-0.3, 0.3]$, with step 0.06

$N_{\text{MC}} = 100$ toy MC samples were generated and fitted for each combination. The most important parameters describing the fit stability are number of successfully fitted samples N_{pass} and the fit uncertainty σ_{fit} . Since the very complicated functions were fitted with a very low statistics, the fit did not pass always successfully ($N_{\text{pass}} \leq N_{\text{MC}}$). The following parameters were computed only from the successfully passed events. The fit error σ_{fit} should scale with $1/\sqrt{n_{\text{ev}}}$; where n_{ev} is a number of signal events ($n_{\text{ev}} \approx n \times r \times n_{\text{Run1}}$). The measured signal yields in Run 1 can be found in Tab. 3.3.

The fit biases are tested by comparison of parameters obtained from the fit with the initial parameters for toy-MC generation, and described by a variable *pull*, defined as:

$$p = \frac{Y_i - Y_{\text{init}}}{\sigma_i} \quad (3.1)$$

In the ideal case, the pull distribution should correspond to Gaussian distribution with zero mean and sigma (RMS) equal to unity. A non-zero mean indicates intrinsic bias on the result of a fit-parameter, while non-unity RMS indicates bias on the fit-parameter uncertainty. The mean and RMS of the pull distribution are thus studied below.

3.4 Results

Graphs are plotted in a rather compact way where x -axis represents the q^2 bins used in the analysis, y -axis initial values of the parameter (that was used in generation of the MC samples), and z -axis value of fitted quantity. Two green bands on both sides represent the range of F_L or S_5 values where f_5 is positive in the full decay-angles phase space. For each q^2 bin there are 3 more bins on the right side, from the top, the maximal, mean and minimal values of a given q^2 bin. In addition, on the σ_{fit} plots another bin is added with value of $\sigma_{fit}^{mean}/\sqrt{n}$. This value should be same for all n in the q^2 bin. The z -axis range and scale is customarily chosen with its middle corresponding to the ideal value, naturally with the exception of N_{pass} , where 100% of passed fits is the ideal case. There is no expected ideal value of σ_{fit} (theoretically value of $\sigma_{fit}^{Run1}/\sqrt{n}$ with statistical uncertainty from Run 1 could be used but it varies with q^2), and therefore medium of the z -scale was phenomenologically chosen as $1/\sqrt{n \times r \times 114}$.

Results presented in this chapter take into account the detector acceptance from Run 1.

3.4.1 Summary of the Toy-MC Studies

This analysis was performed with 100 generated toy MC samples for each tested combination. These samples were fitted and results of the fits were compared with the initial parameters. Four variables were studied in order to examine stability and intrinsic biases of the fit: number of successfully passed fits, parameters fit errors, gaussian mean and RMS of pulls of each of the parameters.

$N_{MC}=100$ was chosen as the best compromise between the relevance of results and the computational time consumed. This contributed to rather large fluctuations (uncertainties) of the results. We expect that sufficient suppression of statistical fluctuations could be achieved by $10 \times$ increasement of N_{MC} . Despite of the fluctuations, there are some visible trends of the fit behaviour for different signal and background yields discussed below. We studied 9 combinations of n and r (however we restricted ourselves for $r = 1$ here in text) in order to establish properties of the fit for possible signal and background yields of Run 2 and HL-LHC. In the following steps of the Run 2 analysis after establishing the yields, the tool-kit developed can be used in a new study focused only on the established yields. Without testing other n - r combination, it would be possible to use $N_{MC}=1000$ with only small increasement of total computational demands.

The analysis of the number of successfully passed fits has the most straightforward interpretation of results, the fit is more stable for regions with higher N_{pass} . Expected increase of N_{pass} with higher number of events was observed in the $[0.04, 2]$ and $[2,4]$ GeV^2 q^2 bins while N_{pass} decreases in the $[4,6]$ GeV^2 bin. This behavior is typical for all parameters F_L , S_3 and S_i for all f_i with acceptance

from Run 1. The instability in the most interesting bin could imply very undesirable consequences for the angular analysis investigating discrepancy between the fit and theory hidden there. The third bin is specific by $2\times$ more background (see tab. 3.3), however, we suppose that different signal and background yields did not caused the instability, since in the first two bins N_{pass} increases for each r , even for $2\times$ more background ($r=0.5$) and results for the $[4,6]$ GeV^2 bin does not improve even for $r=2$ ($n_{\text{sig}}=n_{\text{bck}}$). When we compare results with and without the acceptance, in the results without acceptance the opposite behaviour was observed, not so unambiguous growth or a small decline for the first two bins and expected increase in the third bin. Therefore we conclude that the instability in the $[4,6]$ GeV^2 bin was affected by coefficients of the polynomials describing acceptance (coefficients are specific for combinations of the q^2 bins and functions fitted). This was not deeper investigated yet because of planned modification of the acceptance description in Run 2. Instead of uncorrelated product of polynomials, separated for each angle, three-dimensional spherical harmonical functions will be used.

Values of the fit error are very similar without any significant fluctuations for the whole q^2 bin with more extreme values placed on the edges of tested ranges, where the fit can not estimate its error properly since negative values of functions do not have any probability interpretation and are forced to zero. Values are for the studied parameters F_L and S_5 smallest for the first q^2 bin and highest for the third bin as was established in the Run 1 analysis (Tab. 2 in Ref. [9]). The fit error scales with the number of events as was expected that is demonstrated by the same ratio of $\sigma_{\text{fit}}^{\text{mean}}/\sqrt{n}$ for all n within the q^2 bin.

The ideal values that pull mean and pull RMS would achieve with the infinite statistics are 0 and 1, respectively. Results have rather fluctuating character, but the values do not indicate any larger discrepancies. Average values in the q^2 bins vary around the expected values. The bias on the pull mean is not exceeding value of 1 (i.e. the fit-parameter bias is well below statistical uncertainty). The bias on the pull RMS (i.e. the bias of the fit-parameter statistical error), is typically at the order of 10%, although there are few cases suggesting almost factor of $2 \times$ underestimation of the fit-parameters error, which should be investigated further. Reduction of the biases with increased number of events (n) is not observed, suggesting that even the $100 \times$ larger data sample expected for HL-LHC will be still too small for the complex mass-angular fit to reach the expected zero-bias with infinite statistics.

3.4.2 Plots of Number of Successfully Passed Fits and the Fit Error for F_L with $r=1$ and the Run 1 acceptance

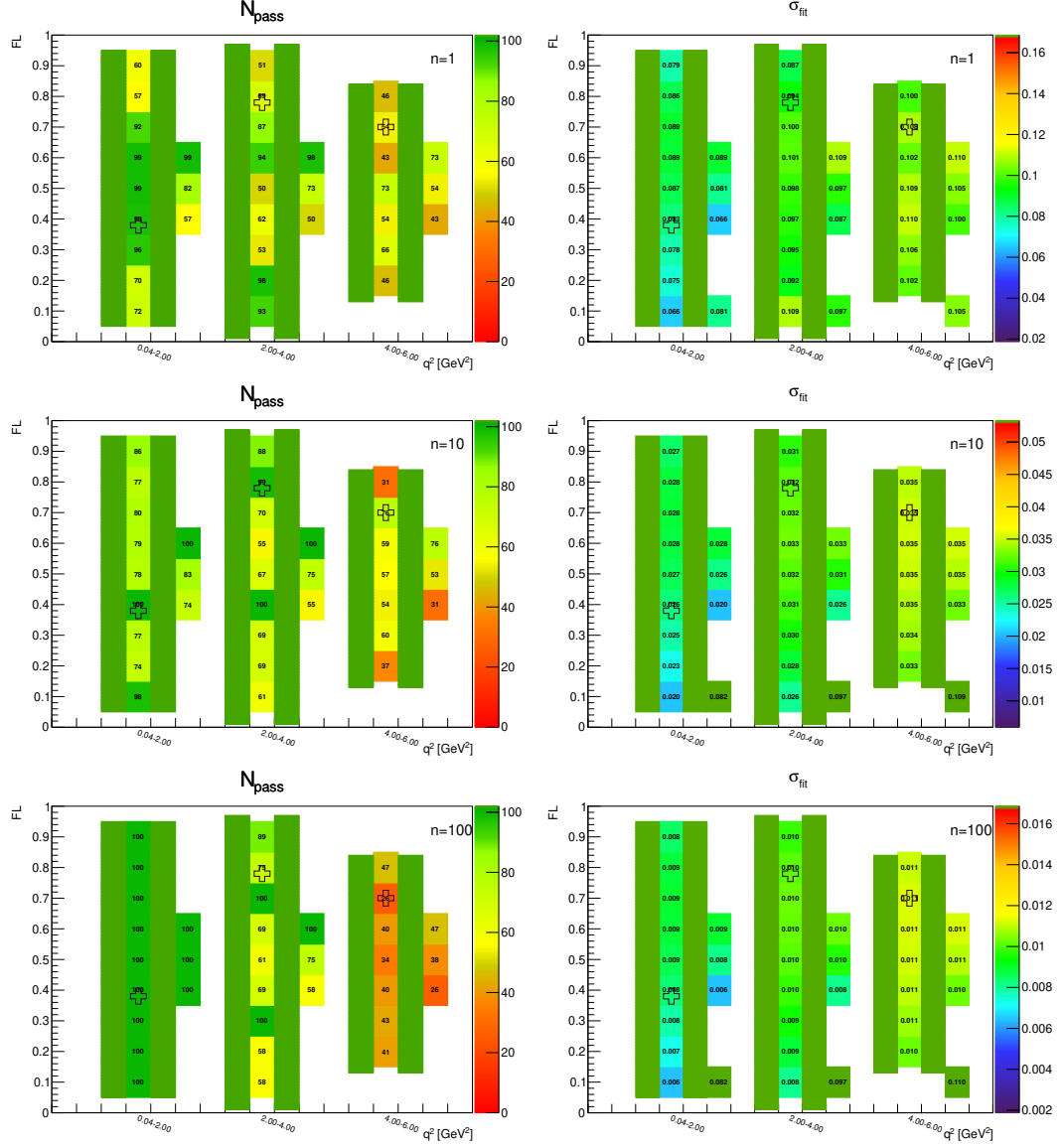


Figure 3.1: Toy-MC studies of the S_5 -fold, with $r = 1$. Figures show the number of successfully passed fits on the toy-MC data (left) and average statistical errors on the parameter F_L (right). The green bands represent fit-p.d.f. positivity range. The top figures correspond to the Run-1 like number of events ($n = 1$), while the middle and the bottom to $10\times$ and $100\times$ larger simulated samples.

3.4.3 Plots of Number of Successfully Passed Fits and the Fit Error for S_5 with $r = 1$ and the Run 1 acceptance

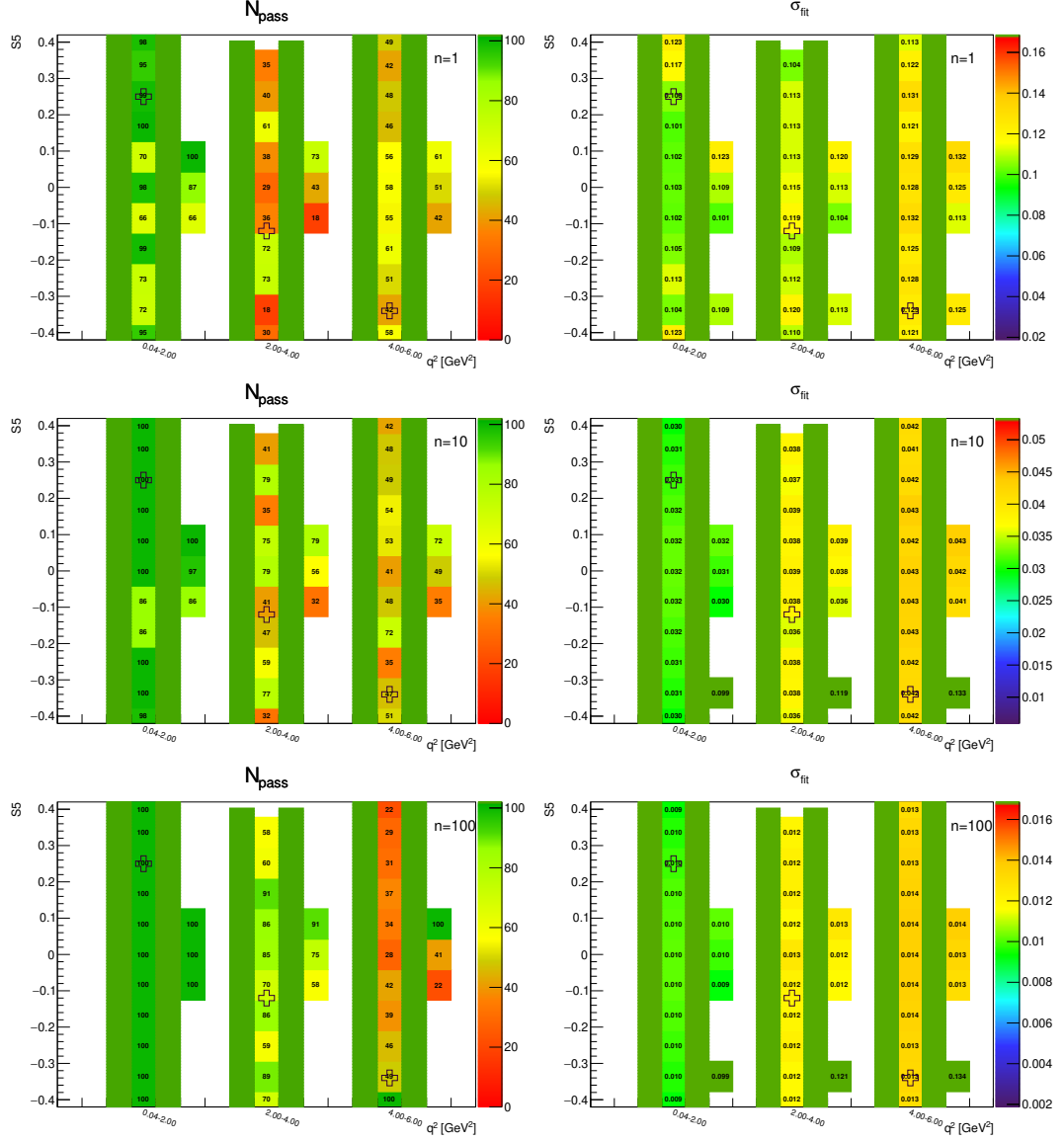


Figure 3.2: Toy-MC studies of the S_5 -fold, with $r = 1$. Figures show the number of successfully passed fits on the toy-MC data (left) and average statistical errors on the parameter S_5 (right). The green bands represent fit-p.d.f. positivity range. The top figures correspond to the Run-1 like number of events ($n = 1$), while the middle and the bottom to $10\times$ and $100\times$ larger simulated samples.

3.4.4 Pull Plots for F_L with $r = 1$ and the Run 1 acceptance

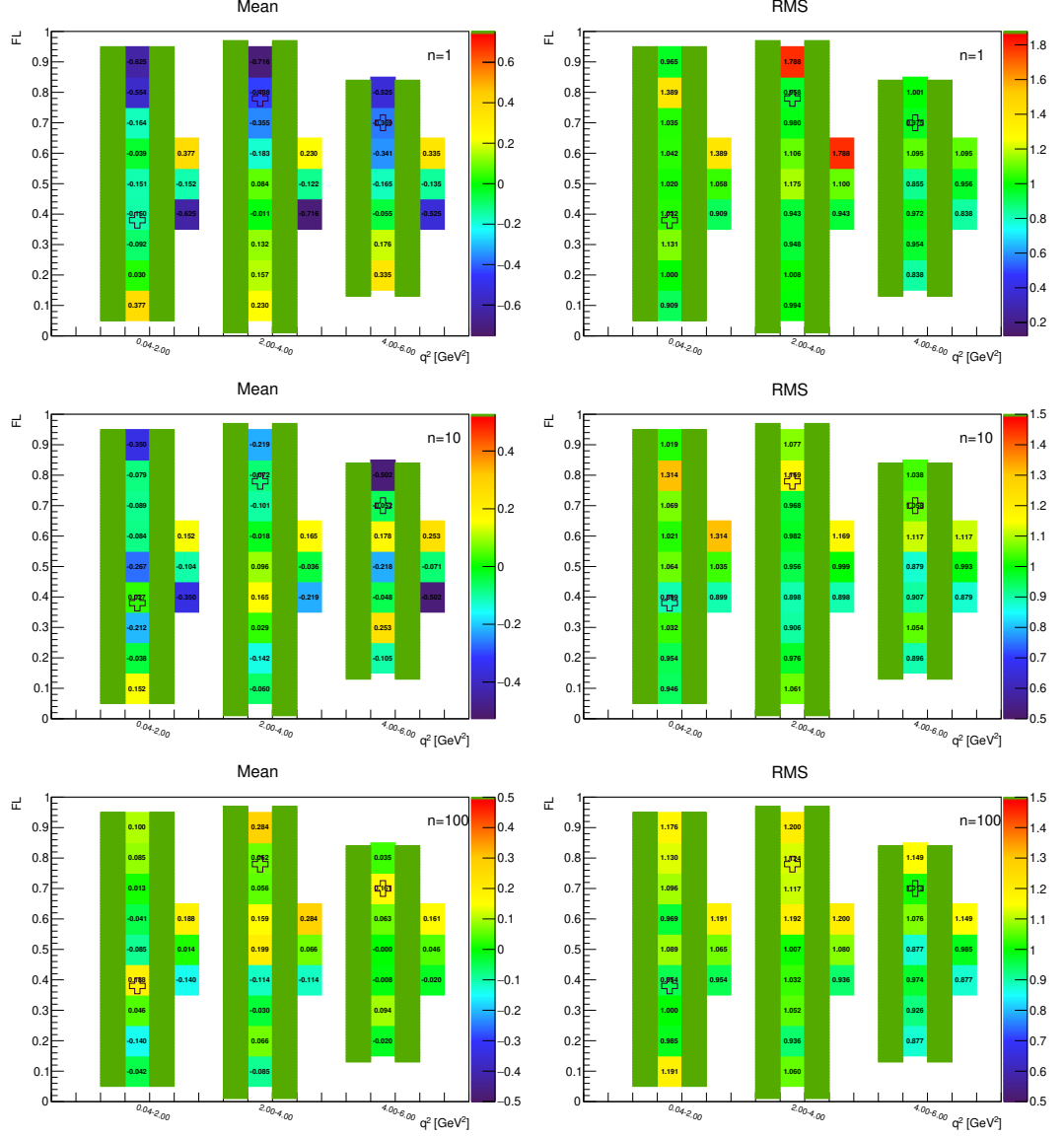


Figure 3.3: Toy-MC studies of the S_5 -fold, with $r = 1$. Figures show the gaussian mean (left) and RMS (right) of pull on the parameter F_L . The green bands represent fit-p.d.f. positivity range. The top figures correspond to the Run-1 like number of events ($n = 1$), while the middle and the bottom to $10\times$ and $100\times$ larger simulated samples.

3.4.5 Pull Plots for S_5 with $r = 1$ and the Run 1 acceptance

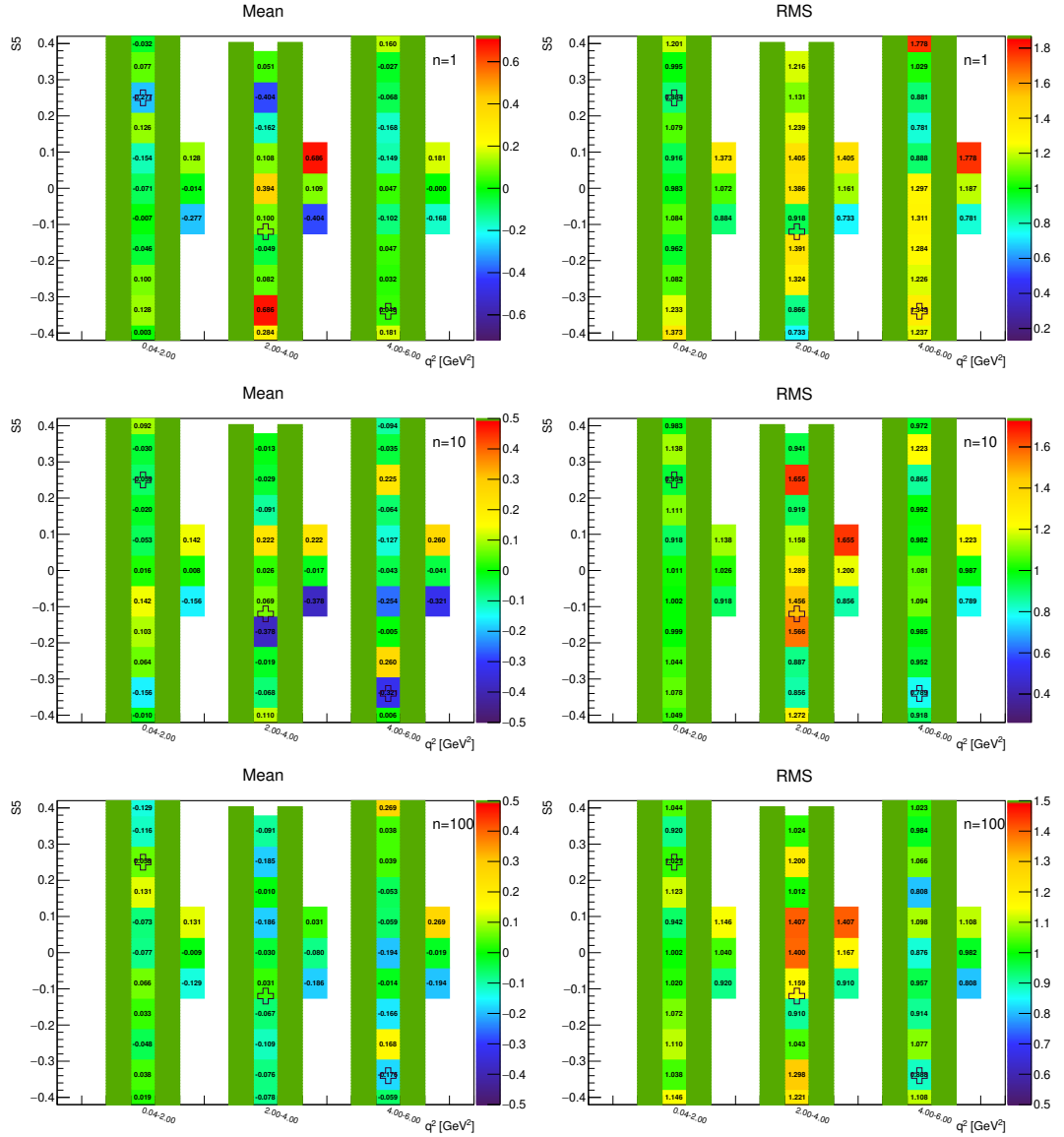


Figure 3.4: Toy-MC studies of the S_5 -fold, with $r = 1$. Figures show the gaussian mean (left) and RMS (right) of pull on the parameter S_5 . The green bands represent fit-p.d.f. positivity range. The top figures correspond to the Run-1 like number of events ($n = 1$), while the middle and the bottom to $10\times$ and $100\times$ larger simulated samples.

4. Events Preselection

The final output from the ATLAS detector are analysis object data (AOD) saving all information about events intended for physics analyses. An individual analysis (or more likely a working group, counting more analyses) choose which data (from the AOD) will be studied, and saves them into derived analysis object data (DAOD). Events are typically selected according to triggers passed or a specific decay signature. Derivation, in addition to preselect events, discards unused information for the analysis (e. g. B -physics analyses normally do not use outputs from the calorimetry and therefore they are removed) and reconstructs physical quantities specific for the analysis (fitting of 4-particle vertex $K\pi\mu\mu$, reconstruction of m_B , m_{K^*} , etc.). DAOD represents an intermediate stage of the events preselection and still contains majority of information that would never be used in the following analysis after the event preselection. Therefore DAOD is again reduced and converted into a ROOT n-tuple, maintaining only physical quantities required for the analysis. Within the process of n-tuple creation, baseline selection criteria are applied in order to suppress majority of background and to ensure a sufficient quality of the measurement.

This chapter is focused on the last step of the events preselection, transformation of the DAOD into the final n-tuple. The software developed is tested on Monte Carlo data which passed the whole reconstruction process as the real data and were saved in the DAOD format. The MC samples of signal and most of background decays (and CP-conjugated antidecays) were used. A next stage of the analysis after the preselection would be the final event selection. In Run 1, simple selection criteria (cuts on chosen variables) were used, in Run 2 there is a plan to use more advanced multivariate techniques (e.g. BDT). However an optimization of selection criteria or BDTs requires the inclusive background taken from the real data (out of the region of interest) which are not available by the time of finishing this thesis. Therefore, the demonstration of the functionality of the developed n-tuple maker software is performed applying optimized criteria from the Run 1 analysis.

The chapter is organized as follows: technical aspects of the work are discussed in Sec. 4.1, baseline and optimized selection criteria of Run 1 are introduced in Sec. 4.2, and Sec. 4.3 is focused on a presentation of results of the selection criteria application. Detailed examination how the cuts effect the number of passed events of the signal decay and antidecay is described in Sec. 4.3.1. Sec. 4.3.2 indicates a rough estimation of expected proportion of background decays to 1 signal event.

4.1 Used Software

AOD and DAOD data are saved in a special data format xAOD [13] that is a new ROOT-readable data format ¹. xAOD includes information about the event (event number, luminosity block, run number, etc.) and about reconstructed objects within each event (tracks, muons, jets, etc.). Information conserved in

¹In Run 1, AODs could not be read by ROOT directly.

the xAOD is split into the object itself and the auxiliary store, containing the numerical values of the object properties (m , p_T , etc.). This enables reading of a given variable across many objects/events with no necessity to load the full event. As all particle objects are stored in containers, it is possible to iterate over particles of the same type in a given event.

All ATLAS production workflows as event generation, detector simulation, reconstruction and derivation production as well as ATLAS High Level Trigger are handled with Athena [14], the ALAS software framework. Measured RAW data or generated MC samples are preprocessed into ESD (Event Summary Data), ESD is processed and saved into AOD from which DAOD is derived. An analysis can be also performed at the Athena level but more often the ROOT-based frameworks are involved. In the second case, instead of using derived dataset (DAOD, which can be read with ROOT on lxplus after launching Analysis-Base [15]) it is a good practise (or rather a necessity) to create ROOT n-tuple with only these information that will be used in the analysis.

For this purpose, software from the $\tau \rightarrow \mu\mu\mu$ analysis [16], based on ELBrain [17] and the PyAnalysisTools [18], was used as a model and was rebuilt into a new class *ELKstarMuMu* within this framework, according to requirements of the $K^*\mu\mu$ and K^*ee analyses. The class is still in progress, however tasks within the scope of this thesis were successfully accomplished. After adaption to connection of different parts of the framework through the Python environment, the class *ELKstarMuMu* was formally prepared beside the original *ELTau3Mu* and reading and saving of following variables was ensured:

- event information (event number, luminosity block, run number),
- variables prepared during derivation (reconstructed masses, B life time, vertex fit quality, refitted primary vertex (PV) position),
- variables computed from them (p_T , η),
- “true variables” for MC samples (flag marking whether the reconstructed decay comes from the real signal decay, “true” positions of PVs).

The AOD contains list of particle tracks and their association primary pp collision vertices. Secondary (B -)vertices are not searched for. Therefore during the derivation, muon pairs with opposite charge and dimuon invariant mass lower than 5500 MeV are firstly refitted into dimuon candidates requiring vertex fit quality: $\chi^2/n.d.f. < 20$. Then B -vertices are formed from the dimuon candidates and two other oppositely-charged tracks not identified as muons. Finally all primary vertices are refitted excluding the 4-candidate tracks [19].

There are more possible approaches to assign a primary vertex from which the B -candidate is expected to originate. The following 3 are typically used: *minimal* a_0 , *minimal* z_0 and *maximal* $\Sigma_i |p_{T_i}|$ where i runs through all tracks coming from the PV, a_0 stands for 3-dimensional impact parameter (distance between line in B -momentum direction pointing from the B -vertex) and z_0 represents distance in the longitudinal direction z along the beam. Maximal $\Sigma |p_T|$ chooses a vertex with the highest energy in the transversal direction that has the highest probability of an “interesting” decay. B -physics adopts the minimal a_0 approach since b -quark production is quite common in pp collisions so B -mesons do not

necessary have to origin in potentially the most interesting pp interaction vertex. Fortunately, the τ_B measurement is rather insensitive to the choice of PV, because the PVs are placed along the z -axis with minimal spread in the transverse (xy) plane, while the B -meson lifetime is calculated using the projections into the transverse plane.

4.2 Selection Criteria

4.2.1 Baseline Cuts

A set of baseline cuts is applied to ensure sufficient quality of the measurement. They are applied at the “n-tuple creation level” so only events passed through these selection criteria are saved. This set is taken from the ATLAS 2011 $B_d^0 \rightarrow K^{*0} J/\psi$ analysis as it has the same final state:

- to account for detector acceptance effects, all four tracks as well as K^* , di-muon and B candidates are required to have rapidity $|\eta| < 2.5$,
- m_{K^*} lays in the interval mean \pm halfwidth: [846, 946] MeV,
- m_B lays in [5150, 5700] MeV,
- trigger requirement: $p_{T\mu} > 3500$ MeV,
- to reduce inaccuracies of the ID: $p_{Tmesons} > 500$ MeV (this cut was applied during the derivation and therefore we do not consider it in the thesis),
- the fit quality of dimuon vertex: $\chi^2/n.d.f. < 10$.

4.2.2 Run 1 Cuts

The selection criteria used in the Run 1 were optimised according to the efficiency defined as $\mathcal{P}(N_{sig}, N_{bckg}) = N_{sig}/\sqrt{N_{sig} + N_{bckg}}$. The specific values of cuts were obtained by the optimization but cutting variables were mostly chosen with respect to the physical motivation:

- $\tau_B/\Delta\tau_B > 12.75$ (The lifetime cut prefers the long-lived B -mesons and suppresses some short-lived hadrons. The cut is applied on lifetime significance to impose quality requirements on the lifetime measurement.)
- $\cos\theta > 0.999$; θ is defined as the angle between the reconstructed direction of flight of B -candidate and its 3-momentum (The cut on the 3D pointing angle θ is used to suppress hadronic background. Ideally, this angle should be equal to zero, but the limited detector resolution is accounted for. Due to technical reasons on the input derivation data, the $\cos\theta$ variable was not available and thus cut was not applied.)
- $p_{TK^*} > 3000$ MeV (comes from optimization).
- The quality of the four track (B -vertex) fit: $\chi^2/n.d.f. < 2$.

- $\Delta m \equiv |(m(B)_{rec} - m(B)_{PDG}) - (m(\mu^+\mu^-)_{rec} - m(c\bar{c})_{PDG})| > 130 \text{ MeV}$; where $c\bar{c}$ represents J/ψ and $\psi(2S)$ (The last cut on a correlation of mass-shifting of B -candidate and dimuon candidate is required to remove radiative charmonium decays from corresponding B -decays as $B_d^0 \rightarrow K^{*0} J/\psi$ followed by $J/\psi \rightarrow \gamma\mu\mu$. The correlation is a consequence of the detector resolution affecting the masses of the B -meson and the charmonium.)

4.3 Results

4.3.1 Application of Selection Criteria

DAOD full-MC samples of the signal decay and antidecay were generated with N_{GEN} events. Each event includes a “true” decay of B_d^0 (\bar{B}_d^0) into K^* (\bar{K}^*) $\mu\mu$ (as well as forcing K^* into charged $K\pi$ decay). Events pass the same reconstruction as the real data in the detector and N_{TOT} decays are reconstructed in $N_{\text{GEN}}^{\text{REC}}$ events. Most of them (N_{B}) do not correspond to the “true” decay and create, so called, self-background (a subset of combinatorial background inside of the signal events). In this section we omit that at this stage there are multiple candidates per event and focus solely on efficiency of the selection criteria. The Tab. 4.1 and 4.2 present:

- N_{S} (N_{B}) – the number of reconstructed signal (self-background) decays
- N_{PASS} – the number of all reconstructed decays passed the corresponding cut and the cuts listed above,
- $N_{\text{S}} / N_{\text{PASS}}$ – the ratio of the signal to the all reconstructed decays (“the cut efficiency”),
- $N_{\text{PASS}}/N_{\text{TOT}}$ – the number of reconstructed decays passed the cut to the number of all reconstructed decays.

In the first line “raw data” are shown all reconstructed decays without application of any selection criteria ($N_{\text{PASS}}^{\text{RAW}} = N_{\text{TOT}}$).

name	N_{S}	N_{B}	N_{PASS}	$N_{\text{S}} / N_{\text{PASS}}$	$N_{\text{PASS}}/N_{\text{TOT}}$:
raw data	8645	66798	75443	0.11	100.00%
$ \eta _{4Btracks}$	8546	64644	73190	0.12	97.01%
dimuon vertex	5319	7052	12371	0.43	16.40%
$p_{T\mu}$	5240	6687	11927	0.44	15.81%
m_{K^*}	4102	2402	6504	0.63	8.62%
m_B	3767	637	4404	0.86	5.84%
τ_B/σ_{τ_B}	1132	454	1586	0.71	2.10%
p_{TK^*}	576	42	618	0.93	0.82%
B vertex	517	22	539	0.96	0.71%
$\Delta m_{radiative}$	374	15	389	0.96	0.52%

Table 4.1: Signal and self-background yield after the application of selection criteria for decay $B_d^0 \rightarrow K^*(K\pi)\mu^+\mu^-$.

name	N_S	N_B	N_{PASS}	N_S / N_{PASS}	$N_{\text{PASS}}/N_{\text{TOT}}$
raw data	8433	64221	72654	0.12	100.00%
$ \eta _{4B\text{tracks}}$	8362	62121	70483	0.12	97.01%
dimuon vertex	5313	7065	12378	0.43	17.04%
$p_{T\mu}$	5246	6719	11965	0.44	16.47%
m_{K^*}	4164	2443	6607	0.63	9.09%
m_B	3317	683	4000	0.83	5.51%
τ_B/σ_{τ_B}	998	478	1476	0.68	2.03%
p_{TK^*}	379	29	408	0.93	0.56%
B vertex	350	22	372	0.94	0.51%
$\Delta m_{\text{radiative}}$	265	13	278	0.95	0.38%

Table 4.2: Signal and self-background yield after the application of selection criteria for decay $\bar{B}_d^0 \rightarrow \bar{K}^*(K\pi)\mu^+\mu^-$.

4.3.2 Background Yield Estimation

The same approach as in the previous section with small modifications is used for the background decays. For background decays, there is no reasonable interpretation of N_S and N_B and therefore only N_{PASS} is used. A next modification for sake of brevity is replacement of partial results for a separate cut by results after application of the whole set of cuts, i.e.:

- $\frac{N_{\text{PASS}}^{\text{baseline}}}{N_{\text{TOT}}}$ – efficiency of the decay reconstruction after application of the baseline cuts during the n-tuple creation,
- $\frac{N_{\text{PASS}}^{\text{Run1}}}{N_{\text{TOT}}}$ – final efficiency of the decay reconstruction after application of the baseline cuts and the cuts from the Run 1 analysis.

To consider efficiency of the decay reconstruction, a new variable is introduced:

- $\eta^{\text{REC}} \equiv \frac{N_{\text{GEN}}^{\text{REC}}}{N_{\text{GEN}}}$, where $N_{\text{GEN}}^{\text{REC}}$ is the number of events with at least 1 reconstructed event.

In order to estimate expected background yields proportional to 1 signal event $\frac{N_{\text{PASS}}^{\text{Run1}}}{N_{\text{TOT}}}$ is multiplied by the factor f defined as follows:

$$f \equiv \frac{f_{B_x} \times BR_{B_x \rightarrow h\mu\mu} \times BR_h \times BR_\mu}{f_{B_d} \times BR_{B_d \rightarrow K^*\mu\mu} \times 2/3 \times 1} \times \mathcal{N} \times \eta^{\text{REC}}; \text{ where}$$

$$\mathcal{N} \equiv \frac{1}{\left(\frac{N_{\text{PASS}}^{\text{Run1}}}{N_{\text{TOT}}} \times \eta^{\text{REC}}\right)_{B_d \rightarrow K^*\mu\mu} + \left(\frac{N_{\text{PASS}}^{\text{Run1}}}{N_{\text{TOT}}} \times \eta^{\text{REC}}\right)_{\bar{B}_d \rightarrow \bar{K}^*\mu\mu}}$$

The first part normalizes the probability of the processed decay to the signal decay, \mathcal{N} factor makes the final expectation to be proportional to 1 signal event (decay or antidecay) and η^{REC} takes into account the reconstruction efficiency.

decay chanel	η^{REC}	N_{TOT}	$\frac{N_{\text{PASS}}^{\text{baseline}}}{N_{\text{TOT}}}$	$\frac{N_{\text{PASS}}^{\text{Run1}}}{N_{\text{TOT}}}$	N_{PASS}	yield
$B_d^0 \rightarrow K^*(K\pi)\mu\mu$	75.8%	75443	5.84%	0.73%	550	0.51
$\bar{B}_d^0 \rightarrow \bar{K}^*(K\pi)\mu\mu$	75.8%	72654	5.51%	0.70%	510	0.49
$B_d^0 \rightarrow K^*(K\pi)J/\psi(\mu\mu)$	74.8%	63052	6.12%	0.03%	21	1.8
$\bar{B}_d^0 \rightarrow \bar{K}^*(K\pi)J/\psi(\mu\mu)$	74.6%	63719	5.44%	0.31%	195	17
$B_d^0 \rightarrow K^*(K\pi)\psi(2s)(\mu\mu)$	74.9%	40605	7.46%	0.04%	16	0.14
$\bar{B}_d^0 \rightarrow \bar{K}^*(K\pi)\psi(2s)(\mu\mu)$	75.5%	42770	6.35%	0.43%	182	1.5
$B_d^0 \rightarrow K\pi J/\psi(\mu\mu)$	58.4%	83092	1.64%	0.04%	36	2.5
$\bar{B}_d^0 \rightarrow K\pi J/\psi(\mu\mu)$	58.5%	40658	1.55%	0.08%	32	4.6
$B_d^0 \rightarrow K\pi\psi(2s)(\mu\mu)$	66.2%	39387	2.80%	0.08%	31	0.36
$\bar{B}_d^0 \rightarrow K\pi\psi(2s)(\mu\mu)$	64.7%	40164	2.28%	0.13%	53	0.58
$B_s^0 \rightarrow \varphi(KK)\mu\mu$	78.1%	152231	1.09%	0.10%	155	0.016
$\bar{B}_s^0 \rightarrow \varphi(KK)\mu\mu$	78.1%	50643	1.03%	0.09%	44	0.013
$B_s^0 \rightarrow \varphi(KK)J/\psi(\mu\mu)$	76.7%	47357	1.06%	0.03%	13	0.33
$\bar{B}_s^0 \rightarrow \varphi(KK)J/\psi(\mu\mu)$	77.3%	45732	1.08%	0.03%	12	0.32
$B_s^0 \rightarrow \varphi(KK)\psi(2s)(\mu\mu)$	77.1%	42756	1.27%	0.04%	18	0.034
$\bar{B}_s^0 \rightarrow \varphi(KK)\psi(2s)(\mu\mu)$	78.1%	43623	1.31%	0.03%	14	0.026
$B^+ \rightarrow K^+\mu\mu$	46.3%	68788	1.40%	0.08%	58	0.025
$B^- \rightarrow K^-\mu\mu$	47.1%	33213	1.16%	0.02%	6	0.006
$B^+ \rightarrow K^+J/\psi(\mu\mu)$	45.5%	66466	1.32%	0.11%	75	4.5
$B^- \rightarrow K^-J/\psi(\mu\mu)$	45.7%	33183	0.95%	0.02%	5	0.61
$B^+ \rightarrow K^+\psi(2s)(\mu\mu)$	45.3%	58200	1.91%	0.11%	64	0.36
$B^- \rightarrow K^+\psi(2s)(\mu\mu)$	45.4%	27965	1.51%	0.03%	8	0.095
$B^+ \rightarrow \pi^+J/\psi(\mu\mu)$	45.9%	32698	1.02%	0.04%	12	0.057
$B^- \rightarrow \pi^-J/\psi(\mu\mu)$	44.9%	31941	0.83%	0.01%	4	0.019
$B_d^0 \rightarrow K^*(K\pi)\eta(\mu\mu)$	79.3%	174749	0.95%	0.15%	261	10^{-5}
$\bar{B}_d^0 \rightarrow K^*(K\pi)\eta(\mu\mu)$	80.6%	90586	1.14%	0.20%	186	10^{-5}
$B^+ \rightarrow \pi^+\eta(\mu\mu)$	65.9%	77825	0.55%	0.03%	23	10^{-7}
$B^- \rightarrow \pi^-\eta(\mu\mu)$	66.9%	79060	0.55%	0.03%	23	10^{-7}
$B^+ \rightarrow K^+\eta(\mu\mu)$	66.2%	79143	0.61%	0.04%	30	10^{-7}
$B^- \rightarrow K^-\eta(\mu\mu)$	66.1%	77576	0.58%	0.03%	20	10^{-7}

Table 4.3: The efficiency of reconstruction, baseline and Run 1 cuts on the signal and background samples. The last row presents the expected number of observed events from the given B -decay per single signal event.

An unexpected result is the asymmetry observed between the estimated background yields for B_d^0 and B^+ decays and their CP-conjugated (anti)decays. The detailed look at the separate cuts showed that the asymmetry appears after cutting on m_B . Later investigation showed that was caused by incorrect reconstruction of mass for $m_{\bar{B}}$ mass hypothesis in the derivations (input datasets for our n-tuple maker).

Our naive estimation of background events results in 36 events but after correction of $m_{\bar{B}}$ in derivations we expect decrease to 12 since there is no reason for asymmetry of yields for decays and their CP-conjugated decays. This will decrease once more after cut on $\cos\theta$ and ϕ -veto on di-muon mass which were not applied yet.

The highest contributions come from decays: $B_d^0 \rightarrow K^* J/\psi(\mu\mu)$, $B_d^0 \rightarrow K^* J/\psi(\mu\mu)$, $B_d^0 \rightarrow K^* \psi(2S)(\mu\mu)$ and $B_d^0 \rightarrow K^* \psi(2S)(\mu\mu)$ because of their structure that is identical as the signal decay. However, an additional veto can be applied on di-muon mass around $c\bar{c}$ resonant peaks J/ψ and $\psi(2S)$ which suppresses them more significantly. This would also reduce higher contributions from $B^\pm \rightarrow K^\pm J/\psi$ (and $B^\pm \rightarrow K^\pm \psi(2S)$). On the other hand decays containing η are naturally suppressed by its branching ratio of the following decay into muons.

Conclusion

Two major tasks connected with the $B_d^0 \rightarrow K^* \mu \mu$ analysis were carried out within this thesis: toy-MC studies of possible intrinsic biases of the B_d -mass and decay-angles fit and development of the framework for creation of reduced dataset (ROOT n-tuple) from initial ATLAS analysis data format (derivation).

The first part examines the fit behaviour for 3×3 combinations of number of expected events and signal-to-background ratio representing possible signal and background yields of the Run 2 and HL-LHC analysis. An emphasis was put on the fit functions involving parameter P'_5 connected with measured deviations from Standard Model by the LHCb experiment. Results for the remaining parameters with and without including the effect of detector acceptance are presented in the appendix. Expected improvement of the fit stability with higher statistics was observed in the $[0.04, 2.0]$ GeV^2 and $[2.0, 4.0]$ GeV^2 q^2 bins. The inverse behavior in the $[4.0, 6.0]$ GeV^2 bin is explained as the result of the acceptance effects. This is a new reason in favour of the planned modification of the acceptance description in Run 2. The fit biases did not decrease with increasing number of events that suggests that even the $100\times$ larger dataset after the HL-LHC update would be still too small to suppress the fit bias. On the other hand, the fit bias remains below the statistical precision and thus the study demonstrated that the systematic uncertainty connected with the fit bias remains under control.

The second part was focused on DAOD transformation into n-tuple containing event information and basic kinematic variables used in the analysis. Functionality of the developed software was demonstrated on transformation of the signal and most important background MC samples (simulated with the full detection process and saved as DAOD) and within that applying the baseline and Run-1 optimized selection criteria. Prediction of the background yields normalized to 1 signal event was estimated according to the Run 1 selection criteria efficiency and corresponding branching ratios of all tested B -decays.

A. Appendices

A.1 CERN Linux and Batch Service

This appendix is devoted to describe some technical capabilities that were required for successful accomplishment of the thesis. Hopefully, it can also help other younger students that starting to work on ATLAS which can use it as a kind of a introductory manual. However, a large piece of information provided here can have a short expiration period, especially technical limits, since CERN tries its best to improve technical background for researchers and enlarge computational capacities.

Every CERN's user gets in addition to CERN's mail also access to many useful software packages that could be accessible through the LXPLUS (Linux Public Login User Service). It is the interactive service to Linux for all CERN's users [<https://lxplusdoc.web.cern.ch/>]. Users can log on to *lxplus.cern.ch* through *secure shell connection (ssh)* in terminal:

```
ssh username@lxplus.cern.ch
```

A new user automatically obtains a home directory in the Andrew file system (AFS) structure of which size can be gradually increased to 10 GB. Available is also a workspace directory that can be activated, able to contain up to 100 GB. The directory structure is as follows:

```
/afs/cern.ch/home(or work)/first_letter_of_username/username
```

The cluster LXPLUS consists of public machines running CC7 (CERN CentOS 7) Linux in 64 bit mode. Users can log on the concrete machine (with a number *XXX*):

```
ssh username@lxplusXXX.cern.ch
```

However it is not recommended since they get automatically connected to the machine with the best response (the lowest CPU load and least number of login sessions) and LXPLUS does not guarantee that individual machines are available at any given time. The maximal computational time per user is limited freely – 40 CPU hours for the last 4 hours. This is enough for using more lxplus machines simultaneously (a couple of tens for our scripts generating and fitting MC samples, but in general it depends on the complexity of problem) in more terminals or through the *screen* command. A user crossing over this limit is warned by e-mail and if he or she keeps running the computations, they will be killed (cca after 30 minutes).

LXPLUS is devoted to interactive work and hence more computational demanding work should be processed on the CERN batch system. LXPLUS works *interactively* and distributes its computational capacity between all connected users *fairly*, while the batch system reserves some amount of computational capacity *only for one user*. The system is based on queues and users have to *wait* to get assigned computational capacity.

A.1.1 Technical Manual

One of very useful things, when one works on remote PC, is using of the *screen* command [<https://www.gnu.org/software/screen/>] that allows to continue running programs after disconnection.

Running *screen* on LXPLUS is a little complicated due to the usage of kerberos authentication, that requires a valid token in order to keep read/write rights on the AFS system. The token expires after user's logout and running program is then not capable writing output files. Keeping the token valid for 24 hours after user log out can be ensured with program *kinit*. A good, although a bit odd, practice for running *screen* on LXPLUS is:

```
ssh user_name@lxplus.cern.ch    #log in lxplus
screen                          #starting screen
                                #remember the lxplus machine id
                                #(lxplusXXX)
ctrl+a+d                        #detach screen
exit                            #log out
ssh username@lxplus.cern.ch     #log in to any lxplus
ssh username@lxplusXXX.cern.ch  #log in to the concrete lxplusXXX
screen -r                       #refresh screen
kinit                           #provide token (requires password)
.\script_name                   #start a script
ctrl+a+d                        #detach screen
```

Setting a shortcut for the host name:

```
ssh lxplus , resp. ssh lxplusXXX
```

is possible by creation of the config file `~/.ssh/config` including:

```
Host lxplus*
  user username
  Hostname lxplus.cern.ch
  ForwardX11 yes
  ForwardX11Trusted yes
```

The program Kerberos (*krb5*) allows a user to log in to LXPLUS without entering the password each time, the password is provided only once after restarting the computer. More about *screen* (more tabs, *kinit* without entering the password) can be found at [<https://hsf-training.github.io/analysis-essentials/shell-extras/screen.html>].

The older batch system on LXPLUS was replaced by HTCondor [<http://batchdocs.web.cern.ch/batchdocs/index.html>] that is controlled through the terminal by following (and many others) commands:

- *condor_submit job.sub* – asking for a computational capacities assignment for running a script specified in the config file *job.sub*
- *condor_q* – show the running state of the jobs (DONE/RUN/IDLE/HELD)
- *condor_wait out/job.log* – warn you after finishing all running jobs
- *condor_hold n* – hold (pause) job(s), they stay in the queue without running
- *condor_release n* – release held job(s) for running
- *condor_rm n* – remove job(s) from the queue

n - can represent the job id, the cluster id or username (removing all jobs from this user). An alternative to *condor_wait* is using of the bash command *watch*, that regularly update change: *watch -n timeperiod_in_seconds condor_q*.

The structure of config file *job.sub* is typically as follows:

```
executable = /totalpath/script_name.sh
arguments  = $(ClusterId) $(ProcId)
output     = logfiles/batchDetail/script_name.$(ClusterId).$(ProcId).out
error      = logfiles/batchDetail/script_name.$(ClusterId).$(ProcId).err
log        = logfiles/script_name.$(ClusterId).log
...

queue
```

Users can also set their requirements:

```
+JobFlavour = "espresso" # maximal time tag
+MaxRuntime = maximal running time of job in seconds
RequestCpus = required number of CPU
...
```

The lines *output* and *error* set output for *stdout* and *stderr* for each job and *log* saves a total preview of all jobs. The output files rewrite the older version.

Uses tags for maximal running time, after which is job automatically terminated, helps the batch system with planning to reserve the needed computational capacities (shorter running time means shorter waiting time as well):

espresso	= 20 minutes	tomorrow	= 1 day
microcentury	= 1 hour	testmatch	= 3 days
longlunch	= 2 hours	nextweek	= 1 week
workday	= 8 hours		

The default settings is *espresso* with 1 slot of CPU, 2 GB of RAM and 20 GB of free space.

The *queue* command pushes the *executable* script into queue to run. There are more ways of using it:

- *queue (without argument)* - push the script once
- *queue N* - push the same script *N* times
- *queue arguments from input_file.txt* - push the script with arguments from input file (separated in columns) as many times as the number of lines the file has

Jobs pushed with a different *queue* have specific *ClusterId* while multiple jobs pushed with the same *queue* are numbered with *ProcId* beginning from 0.

Bibliography

- [1] T. A. Collaboration, *The ATLAS Experiment at the CERN Large Hadron Collider*, Journal of Instrumentation **3** (2008) no. 08, S08003.
<https://doi.org/10.1088%2F1748-0221%2F3%2F08%2Fs08003>.
- [2] M. Kocian, *ATLAS Pixel, Phase 0 (IBL)*, Tech. Rep. ATL-COM-INDET-2012-107, CERN, Geneva, Dec, 2012.
<https://cds.cern.ch/record/1498241>.
- [3] L. Heinrich, *ATLAS Software Tutorial - Trigger Data and how to Analyze it*, <https://indico.cern.ch/event/403126/contributions/956172/attachments/1153704/1657569/SoftwareTutorialTrigger-2015-09-14.pdf>. online: 22. 2. 2020.
- [4] C. ATLAS, *Letter of Intent for the Phase-I Upgrade of the ATLAS Experiment*, Tech. Rep. CERN-LHCC-2011-012. LHCC-I-020, CERN, Geneva, Nov, 2011. <https://cds.cern.ch/record/1402470>.
- [5] C. ATLAS, *Letter of Intent for the Phase-II Upgrade of the ATLAS Experiment*, Tech. Rep. CERN-LHCC-2012-022. LHCC-I-023, CERN, Geneva, Dec, 2012. <https://cds.cern.ch/record/1502664>.
- [6] *Brief ATLAS Informaton*, https://stanford.edu/group/stanford_atlas/4Particle%20Collision%20and%20Detection. online: 31. 10. 2019.
- [7] Particle Data Group Collaboration, C. Patrignani et al., *Review of Particle Physics*, Chin. Phys. **C40** (2016) no. 10, 100001.
- [8] M. Biros, *Bachelor thesis, Study of the Rare B-meson Decay with the ATLAS Experiment*, <https://dspace.cuni.cz/bitstream/handle/20.500.11956/99922/130231775.pdf?sequence=1&isAllowed=y>.
- [9] ATLAS Collaboration, *Angular Analysis of $B_d^0 \rightarrow K^* \mu^+ \mu^-$ Decays in pp Collisions at $\sqrt{s} = 8$ TeV with the ATLAS Detector*, arXiv:1805.04000 [hep-ex].
- [10] LHCb Collaboration, *Measurement of CP -averaged observables in the $B^0 \rightarrow K^{*0} \mu^+ \mu^-$ decay*, arXiv:2003.04831 [hep-ex].
- [11] S. Jäger and J. Martin Camalich, *Reassessing the Discovery Potential of the $B \rightarrow K^* \ell^+ \ell^-$ Decays in the Large-recoil Region: SM Challenges and BSM Opportunities*, Physical Review D **93** (2016) no. 1, .
<http://dx.doi.org/10.1103/PhysRevD.93.014028>.
- [12] ATLAS Collaboration Collaboration, *$B_d^0 \rightarrow K^{*0} \mu \mu$ Angular Analysis Prospects with the Upgraded ATLAS Detector at the HL-LHC*, Tech. Rep. ATL-PHYS-PUB-2019-003, CERN, Geneva, Jan, 2019.
<https://cds.cern.ch/record/2654519>.

- [13] J. Catmore, *The ATLAS Data Processing Chain: from Collisions to Papers*, https://indico.cern.ch/event/472469/contributions/1982677/attachments/1220934/1785823/intro_slides.pdf. online: 22. 2. 2020.
- [14] *ATLAS Athena Guide*, <https://atlassoftwaredocs.web.cern.ch/athena/>. online: 23. 5. 2020.
- [15] *ATLAS Manual - Browsing the xAOD in ROOT*, <https://twiki.cern.ch/twiki/bin/viewauth/AtlasComputing/SoftwareTutorialxAODEDM>. online: 23. 5. 2020.
- [16] *RK* Analysis Code*, <https://gitlab.cern.ch/RKstar/run2analysis>. online: 6. 5. 2020.
- [17] *ELBrain*, <https://elbraindocs.web.cern.ch>. online: 6. 5. 2020.
- [18] *PyAnalysisTools*, <http://cern.ch/PyAnalysisToolsDocs>. online: 6. 5. 2020.
- [19] I. Carli, *PhD thesis, Angular Analysis of the $B^0 \rightarrow K^* \mu^+ \mu^-$ Decay with the ATLAS Experiment*, <http://cds.cern.ch/record/2696422/files/CERN-THESIS-2018-449.pdf>.